Circumglobal Rossby wave patterns during boreal winter highlighted by wavenumber/phase speed spectral analysis

Jacopo Riboldi[1,3], Efi Rousi[2], Fabio D'Andrea[1], Gwendal Rivière[1], and François Lott[1]

[1]Laboratoire de Météorologie Dynamique, École Normale Supérieure, PSL University, Paris, France
[2]Potsdam Institute for Climate Impact Research (PIK), Leibniz Association, Potsdam, Germany
[3]Department of Earth Sciences, Uppsala University, Uppsala, Sweden

Correspondence: Jacopo Riboldi (jacopo.riboldi@geo.uu.se)

Abstract. The classic partitioning between slow-moving, low-wavenumber planetary waves and fast-moving, high-wavenumber synoptic waves is systematically extended by means of a wavenumber/phase speed spectral decomposition to characterize the day-to-day evolution of Rossby wave activity in the upper troposphere. This technique is employed to study the origin and the propagation of circumglobal Rossby wave patterns (CRWPs), amplified Rossby waves stretching across the Northern

5   Hemisphere in the zonal direction and characterized by few, dominant wavenumbers. Principal component analysis of daily anomalies in spectral power allows for two CRWPs to emerge as dominant variability modes in the spectral domain during boreal winter. These modes correspond to the baroclinic propagation of amplified Rossby waves from the Pacific to the Atlantic storm track in a hemispheric flow configuration displaying enhanced meridional gradients of geopotential height over midlatitudes. The first CRWP is forced by tropical convection anomalies over the Indian Ocean and features the propagation

10   of amplified Rossby wave packets over northern midlatitudes, while the second one propagates rapidly over latitudes between 35°N and 55°N and appears to have extratropical origin. Propagation of Rossby waves from the Atlantic eddy-driven jet to the African subtropical jet occurs for both CRWPs following anticyclonic wave breaking.

1 Introduction

Most of the weather affecting northern midlatitudes has its dynamical origin in the Atlantic and Pacific storm track regions,

15   located to the east of the main continental landmasses and characterized by a particularly strong meridional temperature gradient (e.g., Chang et al., 2002; Hakim, 2003). The majority of extratropical cyclones form and track in those regions while being steered by large-scale atmospheric oscillations, known as Rossby waves, constituted by equatorward (troughs) and poleward (ridges) displacements in the jet stream (Rossby, 1940; Lee and Held, 1993; Wirth et al., 2018). The position and the activity of the Pacific and Atlantic storm tracks, in terms of number, amplitude and propagation of Rossby waves populating them,

20   can vary substantially across a season or between one year and the other (Grise et al., 2013; Hoskins and Hodges, 2019a, b). Understanding the mechanisms governing this variability is a traditional field of research in weather and climate dynamics.

A possible division of this research field could involve a distinction between mechanisms that affect single storm tracks and mechanisms that feature a connection between the two. An example of internal mechanism is the complex role played by background baroclinicity in enhancing, but also in suppressing, storm track activity (Schemm and Schneider, 2018; Schemm

25   et al., 2021). The onset of atmospheric blocking events, characterized by the sudden inflation of large anticyclones that disrupt the usual, eastward Rossby wave propagation, can also be seen as an internal phenomenon affecting storm track variability (e.g., Shutts, 1983; Altenhoff et al., 2008; Martineau et al., 2017; Ferranti et al., 2018). On the other hand, many large-scale flow patterns feature a coordination between the two storm tracks. There is robust evidence that low-frequency tropical forcing, as the El Nino-Southern Oscillation (ENSO) or the Madden-Julian Oscillation (MJO), manifests itself first in anomalies

30   over the North Pacific storm track that are subsequently propagated, via the forcing of transient Rossby waves, to the North Atlantic storm track (Cassou, 2008; Henderson et al., 2016; Zheng et al., 2018; Schemm et al., 2018; Gollan et al., 2019). However, interaction between the two storm tracks can also result from purely extratropical forcing, as baroclinically-induced wave resonance (Yang et al., 1997; Franzke et al., 2006). Such interplay is also related to hemispheric-scale, extratropical teleconnection patterns, like the Northern Annular Mode (e.g., Woollings and Hoskins, 2008; Rivière and Drouard, 2015) or

35   the Northern Baroclinic Annular Mode (Thompson and Li, 2015).

Another circulation pattern that involves a coordination between the two storm track are the so-called circumglobal Rossby wave patterns (CRWPs), that can occur if the large-scale flow configuration is conducive to the zonal propagation of Rossby wave packets (RWPs) over long distances. Concomitant summer temperature extremes in different regions of the Northern Hemisphere have been linked to the occurrence of stationary, amplified, quasi-resonant planetary Rossby waves (Petoukhov

40   et al., 2013; Coumou et al., 2014; Kornhuber et al., 2017, 2019; Xu et al., 2021). During boreal winter, on the other hand, CRWPs stretching across the hemisphere feature an interconnection between the Pacific and the Atlantic storm track and an interplay between the polar and the subtropical jet streams (Branstator, 2002; Franzke et al., 2006; Davies, 2015). In particular, Davies (2015) described how the repeated propagation of a Rossby wave train from the Pacific to the Atlantic storm track, and then back to the Pacific storm track via the subtropical jet stream, shaped the hemispheric wave pattern during winter

45   2013/14 causing widespread extreme weather. This so-called "weather chain" involved the repeated enhancement of RWPs with the same phase and an interaction between the polar and subtropical jet to ensure circumglobal connectivity, and occurred in conjunction with anomalous North Pacific sea surface temperatures (Wang et al., 2014; Hartmann, 2015).

It has been argued that anthropogenic global warming would make the large-scale flow configuration more favorable to the development of amplified Rossby wave patterns at the hemispheric scale (Mann et al., 2018; Teng and Branstator, 2019).

50   Besides the difficulties often encountered while trying to isolate changes in rare events from long-term climate trends, it is arguable that another important issue is of theoretical nature: the current theory of Rossby waves inevitably encounters problems when trying to describe the highly nonlinear flow configurations associated with extreme weather events, as large-amplitude Rossby waves, wave breaking or atmospheric blocking. Recent research work (Wirth, 2020; Wirth and Polster, 2021) discussed the limitations of the Rossby wave ray tracing approach (cf. Hoskins and Karoly, 1981; Hoskins and Ambrizzi, 1993),

55   based on the Wentzel-Kramers-Brillouin (WKB) approximation, when applied to evaluate Rossby wave "waveguidability" at the hemispheric scale and pointed out the need of alternative frameworks to study Rossby wave characteristics in the context of extreme events.

This piece of work proposes wavenumber/frequency spectral analysis as an alternative, versatile tool to describe the variability in shape and stationarity of the midlatitude flow, without having to make a-priori assumptions about the existence of a

background flow in which the waves propagate or about the existence of dominant wavenumbers. This approach can be applied to standard gridded model or reanalysis output with minimal pre-processing and without filtering. This technique is employed routinely to diagnose equatorial waves and other circulations existing in the tropical region (e.g., Wheeler and Kiladis, 1999; Lott et al., 2009), but has not encountered analogous success when applied to the extratropics. Previous applications of this technique to the midlatitudes have mainly described the climatological characteristics of Rossby waves or their differing representation in climate models (e.g., Dell'Aquila et al., 2005). Recent work (Sussman et al., 2020; Riboldi et al., 2020; Jolly et al., 2021) employed space/time spectral analysis to model and assess the presence of trends in the properties of Rossby waves, confirming its usefulness and applicability to climate change problems.

This study consists of an exploration of Rossby wave variability from the spectral perspective, with a particular focus on CRWPs over the Northern Hemisphere during winter. We show that hemispheric-scale Rossby wave patterns dominated by few, selected wavenumber/phase speed harmonics appear as basic modes of variability in the spectral domain, allowing CRWPs to emerge and their evolution to be characterized. The paper is structured as follows: after a description of the approach in terms of spectral analysis and of the employed diagnostics, the patterns of spectral variability and their associated large-scale circulation signatures are discussed in general (Sec. 3) before focusing specifically on the characteristics of the CRWPs highlighted by the spectral analysis (Sec. 4). Conclusions are summarized in Sec. 5, together with an outlook about further possible applications of space/time spectral analysis in the context of climate dynamics.

2 Data and methods

The analysis is based on ERA-Interim Reanalysis data (Dee et al., 2011) between March 1979 and February 2019, for a total length of 40 years. Spectral decomposition is performed using a rapid Fortran-based fast Fourier transform module, developed in 1967 at MIT Lincoln Laboratory by Norman Brenner, Charles Rader and Ralph Alter (Cooley and Tukey, 1965). Daily MJO data for the considered period are obtained from the web page of the Australian Bureau of Meteorology (http://www.bom.gov.au/climate/mjo).

2.1 Wavenumber/phase speed spectral analysis

Spectral analysis allows a decomposition of a given function over a basis of periodic harmonics: in this work, each harmonic corresponds to a propagating sinusoidal wave with zonal wavenumber n and phase speed c_p. These harmonics are obtained from an interpolation, performed at each latitude ϕ, of the wavenumber/frequency harmonics (n,ω) resulting from space/time spectral analysis.

In the first step a double spectral analysis, in space and time, is performed over the ERA-Interim data set of 250 hPa meridional wind anomalies $V'(\lambda,t)$, with six-hourly resolution between January 1979 and December 2019 and spatial resolution of $0.75° \times 0.75°$. Such anomalies are computed with respect to the daily cycle of meridional wind, further smoothed over a 30-day time window. The employed temporal and spatial resolution can resolve harmonics of minimal zonal wavelength of $1.5°$ and minimal frequencies corresponding to an oscillation period of 12 h. This level of detail allows a precise depiction of Rossby

waves associated with rapid transients like, e.g., moving extratropical cyclones (Wheeler and Kiladis, 1999; Dell'Aquila et al., 2005).

The flow is decomposed on each latitude circle as a linear superposition of monochromatic, zonally propagating waves

$$V'(\lambda, t) = \sum_{j=-N_T/2}^{N_T/2} \sum_{n=-N_L/2}^{N_L/2} \hat{V}'(n, \omega_j) e^{i(n\lambda - \omega_j t)} \tag{1}$$

where $\hat{V}'(n, \omega_j) \in \mathbb{C}$ are the spectral coefficients, λ represents longitude and t is time, $N_L = 480$ is the number of grid points along a given latitude circle on the considered grid and $\omega_j = 2\pi j / N_T$ is the frequency, ranging in a time window of 61 days (containing $N_T = 244$ six-hourly time steps). The spectral analysis was performed in a sliding two-month time window centered on each day between the 1st of February 1979 and the 30th of November 2019. A double cosine tapering is applied to the first and last 12 days of the time series to minimize Gibbs effect. The modules $\hat{V}'\hat{V}'^{*}$ of the complex coefficients obtained from the spectral analysis constitute the so-called periodogram: by Parseval's identity, each value of the periodogram is proportional to the variance of the meridional wind anomalies explained by the corresponding (n, ω_j) harmonic. Following Wheeler and Kiladis (1999), each periodogram is smoothed 10 times in frequency using a three-point window.

The periodogram is then interpolated along lines of constant phase speed $c_p = \frac{\omega a \cos\phi}{n}$, where a=6.371·10^6 m is the Earth's radius, to obtain wavenumber/phase speed spectra $S(n, c_p, \phi)$. Following the approach by Randel and Held (1991), the interpolation is performed on a range of phase speeds between -30 m s^{-1} and +30 m s^{-1} in steps of $\Delta c_p =$1 m s^{-1}. This implies that the harmonics with phase speed $|c_p| <$1 m s^{-1} or $|c_p| >$30 m s^{-1} at each latitude are excluded. Harmonics with c_p=0 m s^{-1} are also not represented, because they correspond to waves with null frequency and, therefore, infinite period. The periodograms are multiplied by a wavenumber- and latitude-dependent scaling factor $\frac{n}{a \cos\phi}$ before interpolation to preserve variance during the coordinate change (cf. Randel and Held, 1991).

As a final step, a global estimate $\overline{S}(n, c_p)$ of the Rossby wave spectrum over midlatitudes is obtained by averaging together the phase speed spectra computed for each latitude between 35.25°N and 75°N (every 0.75°). This broad latitudinal range has been chosen 1) to take into account possible nonzonal propagation of Rossby waves and 2) to account for intraseasonal and interannual latitudinal variations in Rossby wave propagation and storm track activity. An alternative approach would have consisted in performing first the latitudinal average of the wind anomalies and then a single spectral analysis, as in Dell'Aquila et al. (2005): however, this would have blurred the description of wave breaking/atmospheric blocking configurations, where wind and geopotential anomalies are often stacked one above the other at the same longitude (some blocking identification mechanisms rely exactly on this property, e.g., Tibaldi and Molteni, 1990; Pelly and Hoskins, 2003; Davini et al., 2012). Furthermore, the averaging over different latitudes acts as a low-pass filter in wavenumber and allows to obtain "smoother", less noisy spectra.

Although a spectrum is attributed to every single day, it is important to precise that each spectrum results from an analysis over a time interval of 61 days (37 if we exclude the tapered days), with a substantial overlap between consecutive days. Despite this apparent limitation, however, the results outlined in this work indicate that the methodology is able to sample a notable intraseasonal variability and to precisely pinpoint time periods of anomalous spectral activity at the daily to weekly scale.
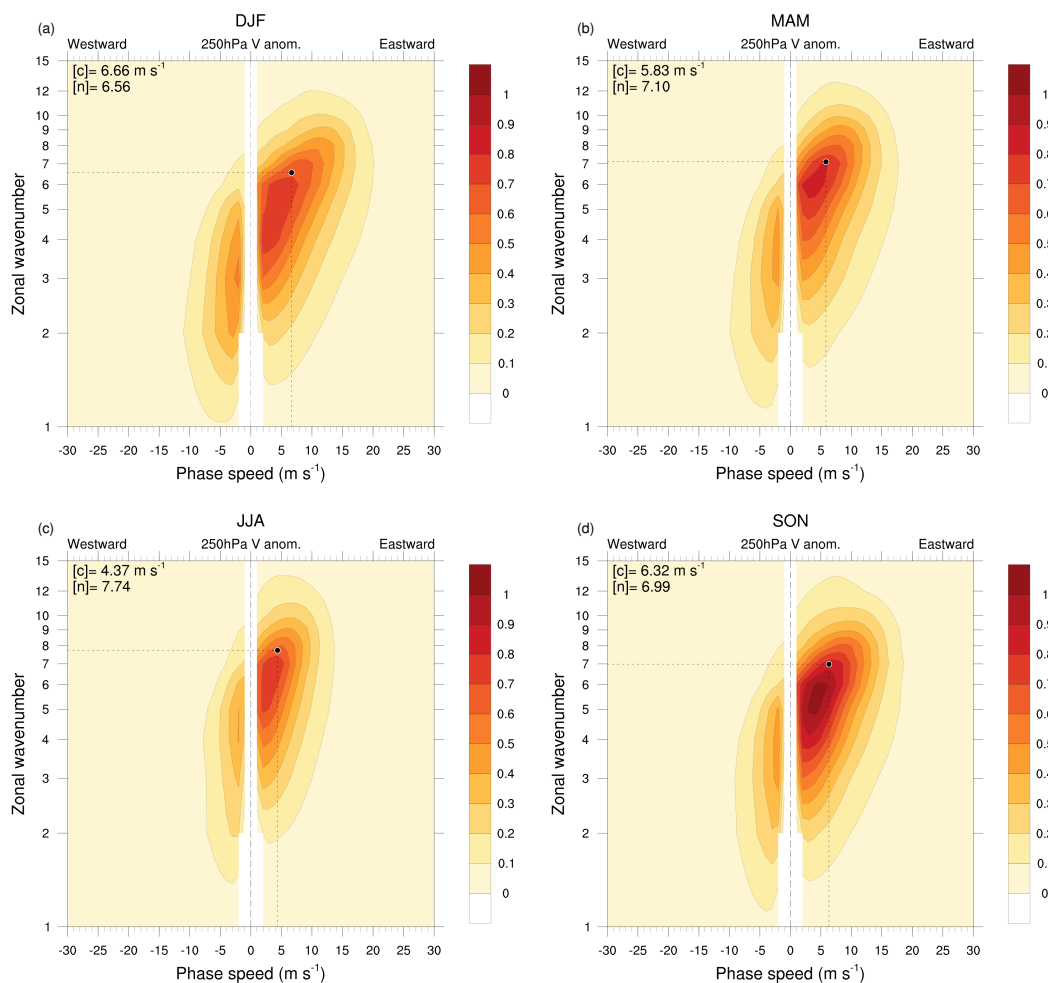
Figure 1. Mean of daily wavenumber/phase speed spectra of meridional wind anomaly at 250 hPa, computed along each latitude circle between 35.25°N and 75°N, every 0.75°N, during the four seasons: (a) DJF, (b) MAM, (c) JJA and (d) SON. Units of spectra is $\mathrm{m\,s^{-1}\,\Delta c^{-1}}$, where $\Delta c = 1\,\mathrm{m\,s^{-1}}$ at 55°N. Black dots indicate the phase speed $[c]$, as in Riboldi et al. (2020), and the average wavenumber $[n]$ expressed as weighted mean with respect to spectral power: the corresponding values are reported in the top left corner of each plot.

125   All the daily spectra can be averaged to obtain seasonal mean spectra, highlighting some basic characteristics as well as the seasonal cycle of $\overline{S}(n, c_p)$ across the different harmonics (Fig. 1). As intuitively expected, the average spectra are not symmetric: more power is present for eastward-propagating waves than for westward ones, with a maximum at wavenumbers n=5-7 depending on the season. High wavenumbers tend to exhibit more power in harmonics with high phase speed as predicted by the Rossby wave dispersion relationship. However, westward-propagating waves are also active for most wavenumbers

130 below n =8, and they reach their maximum power during winter. The distribution of $\overline{S}(n, c_p)$ is flattened around the c_p=0 m s^{-1} line during summer: this indicates that the Rossby wave pattern governing weather conditions over Northern Hemisphere midlatitudes is, on average, more stationary during summer than in winter. The involved wavenumbers are also generally higher during summer, with intermediate values across the transition seasons (MAM and SON). In the rest of the paper, we will only focus on the spectral analysis of boreal winter (DJF).

135 **2.2   Dynamical diagnostics**

The circulation patterns associated to spectral variability modes are described making use of standard meteorological variables such as potential vorticity (PV), geopotential height and zonal wind. More elaborated diagnostics are also employed in the paper, as atmospheric blocking frequency, baroclinicity, transient meridional heat flux, and the **E** vector to diagnose propagation and tilt of transient waves. These less straightforward metrics are described in the following paragraphs.

140 **2.2.1   Atmospheric blocking**

The anomaly-based blocking diagnostic by Schwierz et al. (2004) is employed in this study. In this framework, atmospheric blocking corresponds to a negative anomaly of vertically averaged PV (500-150 hPa, anomalies computed with respect to monthly climatology). After smoothing with a two-day running mean, blocking is identified as a closed region with a negative PV anomaly lower than -1.3 PV units (PVU, $1\,\mathrm{PVU} = 10^{-6}\,\mathrm{K\,m^2\,kg^{-1}\,s^{-1}}$). Furthermore, this region must fulfill an overlap

145 criterion: the minimum spatial overlap of two closed regions delimited in two subsequent 6-hourly time steps must be 70% for at least 5 consecutive days.

    The output of this diagnostic is a two-dimensional boolean (0-1) field: composites of blocking frequency can be computed by determining the percentage of time steps where each grid point was occupied by a blocking. Anomalies in blocking frequency value are then obtained by subtracting the climatological blocking frequency, evaluated over all considered winter days between

150 December 1979 and February 2019.

2.2.2   Rossby wave packet amplitude

The amplitude of Rossby wave packets in the wavenumber range $n = 4-15$ is evaluated at each grid point using the diagnostics by Zimin et al. (2006). To account for the possible non-zonal proagation of Rossby waves, the 250 hPa wind component orthogonal to a local approximation of the background flow (here, a streamline of the mean wind averaged in a time window

155 or 28 days centered at the date of interest) is employed in the computation. This orthogonal wind component is first tapered

in space using a Gaussian filter centered at the grid point of interest and then filtered using a Fourier transform to retain only the considered wavenumbers. The modulus of the inverse Fourier transform of the filtered wind is then the local amplitude of the identified Rossby wave packet envelope. As it represents an amplitude, this metric is positive definite and is not affected by cancellation problems, due to phase shifts between ridges and troughs in the wave packet, when averaging different time steps together. As noticed by Riboldi et al. (2019), this metric does not follow a Gaussian distribution: standardized anomalies of RWP amplitude are then computed with respect to the amplitude logarithm.

2.2.3 Baroclinicity and transient meridional heat flux

The relationship of the identified spectral variability modes with local and global baroclinicity is assessed using the metric developed by Hoskins and Valdes (1990) and employed, among others, by Ambaum and Novak (2014) to study its relationship with meridional heat flux over the North Atlantic storm track.

The baroclinicity metric is essentially a version of the Eady growth rate for unstable baroclinic modes, evaluated at each grid point from the 7-day running averages of zonal wind ($\overline{u}$), meridional wind ($\overline{v}$) and potential temperature ($\overline{\theta}$):

$$s = 0.31 \frac{f}{\overline{N}} \left| \frac{d\overline{\mathbf{V}}}{dz} \right| \tag{2}$$

where f is the Coriolis parameter,

$$\left| \frac{d\overline{\mathbf{V}}}{dz} \right| = \sqrt{\left(\frac{\partial \overline{u}}{\partial z} \right)^2 + \left(\frac{\partial \overline{v}}{\partial z} \right)^2} \tag{3}$$

is the average wind shear magnitude and

$$\overline{N} = \sqrt{\frac{g}{\overline{\theta}} \cdot \frac{d\overline{\theta}}{dz}} \tag{4}$$

the average stratification. Vertical derivatives are evaluated using centered finite differences between $700\,\mathrm{hPa}$ and $850\,\mathrm{hPa}$, so that the value of s refers to the $775\,\mathrm{hPa}$ level. Differently from Ambaum and Novak (2014), time-averaged quantities have been employed to better represent the environmental baroclinicity in which transients are evolving.

The meridional heat flux associated with transient eddies (v^*T^*) is computed at each time step and grid point as the product of transient wind and temperature components at 700 hPa, both obtained by removing the corresponding 7-day running mean of wind and temperature. A seven-day running average is then applied to this instantaneous quantity to better compare it with the baroclinicity metric.

2.2.4 E vector

The propagation and the tilt of transient eddies at the level of the jet stream are diagnosed using the $\mathbf{E}$ vector (Hoskins et al., 1983; Trenberth, 1986) in the formulation by Schemm et al. (2018)

$$\mathbf{E} = (E_x, E_y) = \left[\frac{1}{2} \left(\overline{v^{*2} - u^{*2}} \right), -\overline{u^*v^*} \right] \tag{5}$$

where the transient 250 hPa wind components u^* and v^* are again defined with respect to the 7-day running averages. The

185 two components of the **E** vector for that same day are computed every 6 hours and then averaged to obtain a daily mean value (as indicated by the overbar). The horizontal component E_x is linked to the group speed of transient eddies and can be used to diagnose the preferred direction of propagation of wave energy. The meridional component E_y is linked to the tilt of transient eddies: equatorward-pointing **E** vectors indicate anticyclonically tilted eddies, while poleward-pointing **E** vectors indicate a cyclonic tilt. Furthermore, as hinted by the similarities of E_y with the momentum flux, the divergence of **E** corresponds to

190 transfer of zonal momentum from the eddies to the mean flow. Given these analogies, the meridional component of the **E** vector will be employed here as a proxy of Rossby wave breaking.

3 Variability in the spectral domain during boreal winter

The variability in the distribution of spectral power across the different (n, c_p) harmonics is investigated with empirical orthogonal functions (EOFs) for boreal winter only (DJF). As a first step, spectral anomalies are computed with respect to the

195 climatological seasonal cycle of spectral power. This is obtained by computing the average spectra for each calendar day and then by applying over it a 30-day running mean. Once the anomalies have been computed, standard Principal Component (PC) Analysis is performed over the 3610 winter days between December 1979 and February 2019. The resulting EOFs are consequently patterns of variability in the (n, c_p) space, corresponding to the enhancement of selected harmonics with a given zonal scale and propagation.

200 ### 3.1 EOF patterns

The three first EOFs explain together almost a third of the total variance in spectral space (31.56%, sum of respectively 12.54%, 9.97% and 9.05%); they are presented, together with the associated standardized PCs, in Fig. 2. The first EOF shows a compact maximum for the harmonics which already feature the highest average spectral power during DJF, the ones encompassing wavenumbers n =4-6 and weakly positive phase speeds (Fig. 1a). Positive values of the associated principal component (PC1)

205 correspond to a particular enhancement of such harmonics, while the opposite holds for negative values: we notice that the distribution of PC1 is skewed towards positive values, meaning that positive peaks have usually higher magnitude than negative ones (Fig. 2b). Eastward propagating n =4-6 harmonics sit somehow in the middle between the classical planetary and synoptic wave subsets and have already been shown to be involved in circumglobal teleconnections during DJF (e.g., Branstator, 2002; Davies, 2015). The second EOF features a dipole in variability reminiscent of the distinction between planetary waves, having

210 low wavenumber and phase speed, and synoptic waves, having high wavenumbers and rapidly propagating eastward (Fig. 2c). The positive phase of the associated PC2 features a distinct maximum in spectral power for zonal wavenumbers n =6-8. The excited harmonics have also higher phase speeds than PC1, indicating an overall more rapid eastward propagation of the wave pattern. The third EOF exhibits a tripole of anomalies in the spectral domain, where harmonics having very low (n =2, 3) and high (n =6-8) wavenumber co-variate together with an eastward propagating wave 5 (Fig. 2e). As for PC1, the distribution of

215 PC3 is skewed to the right (Fig. 2f).
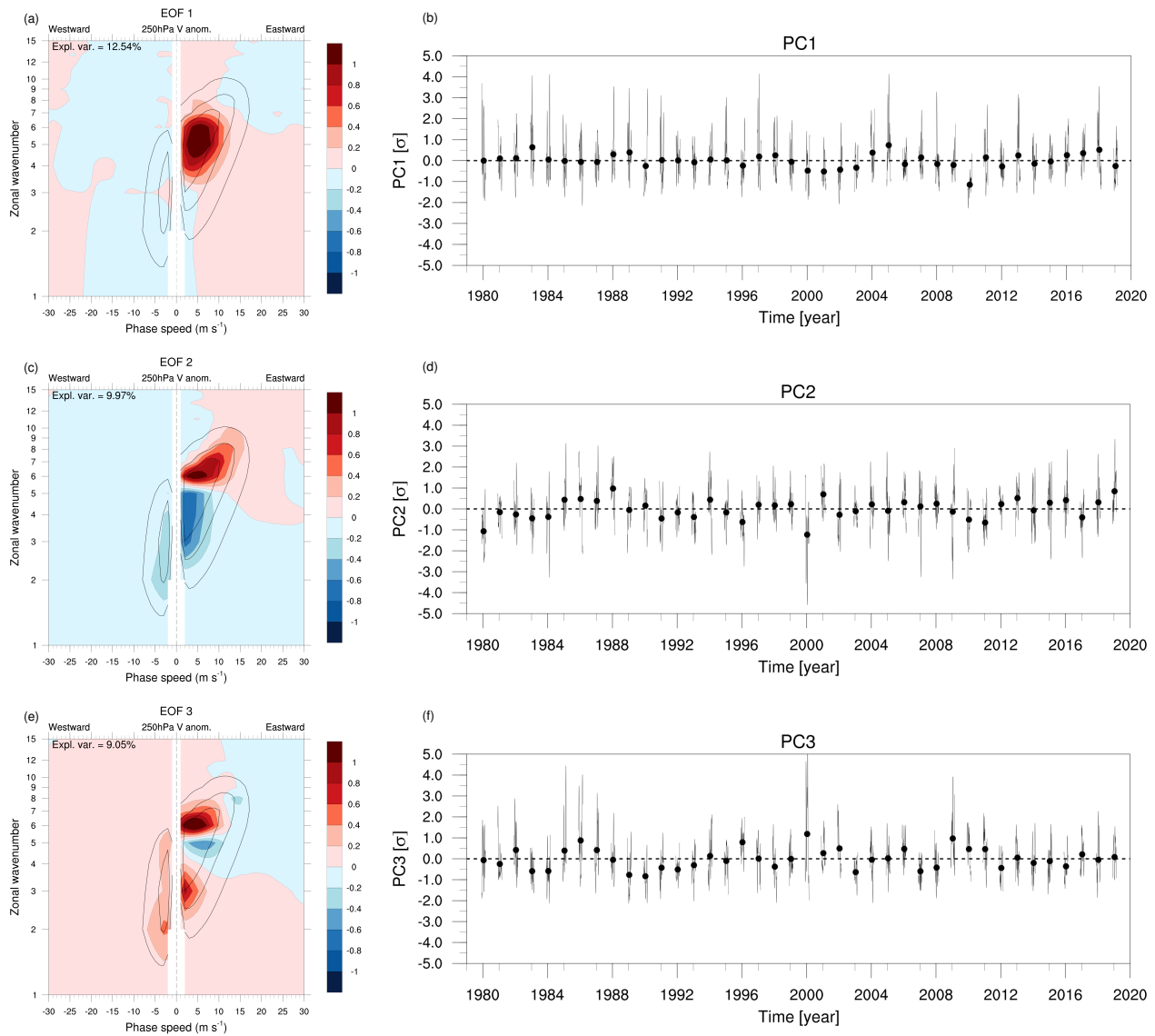
Figure 2. (a,c,e) Loadings of the first three EOFs of daily spectral anomaly during DJF (shaded, arbitrary units). The climatological spectral power is overlaid (black contours as in Fig. 2, only the 0.2, 0.4 and 0.6 $\mathrm{m\,s^{-1}\,\Delta c^{-1}}$ levels). (b,d,f) Principal components associated with each EOF (standardized).

3.2 Circulation anomalies regressed from PCs

A regression analysis linking each PC with daily 250 hPa geopotential height, atmospheric blocking and RWP amplitude anomalies is performed to highlight the main circulation features associated with each spectral variability pattern. The positive phase of PC1 corresponds to an enhanced geopotential gradient over the Pacific and the Atlantic storm track, with a poleward-shifted jet stream (Fig. 3a). The higher latitude of the subtropical anticyclones is highlighted by the positive blocking frequency anomalies at lower latitudes than climatology (Fig. 3b). Notably, these blocks do not appear to be associated with a reversal of the meridional geopotential gradient over the midlatitudes, but instead with slow-moving ridges located between 35°N-55°N, detected as blocking by the Schwierz et al. (2004) identification algorithm (Fig. 3b). Perhaps the most remarkable feature associated with a positive PC1 phase is the simultaneous positive anomalies of RWP amplitude over the whole midlatitudes (Fig. 3c). These amplified Rossby waves are slowly propagating eastward, as they project on harmonics with $c_p < 10 \, \mathrm{m \, s^{-1}}$.

The positive phase of PC2 features an overall increased meridional geopotential gradient and reduced atmospheric blocking activity, in particular over the North Atlantic (Figs. 3d,e). The relationship of this PC with blocking is also proven by a significant anti-correlation with the daily time series of blocking area over the Northern Hemisphere (r=-0.53, $p < 0.01$). While PC1 is associated with a pulsation in RWP amplitude, PC2 seems more related to a latitudinal shift: positive PC2 values are related to enhanced RWP amplitude across midlatitudes, although at more southern latitudes than PC1, and with reduced amplitudes over high latitudes (Fig. 3f). The southward shift in Rossby wave activity is likely related to the equatorward displacement of the Icelandic and Aleutian lows, possibly associated with the positive geopotential height anomalies above the North Pole.

The positive phase of PC3 is associated with a reduction of meridional geopotential gradient and with atmospheric blocking, in particular over the North Atlantic (Figs. 3g,h). Two separate regions of positive RWP amplitude anomalies are observed if PC3 is positive, one over high latitudes (north of 60°N) and one at lower latitudes (below 45°N). This split in RWP pathways suggests the presence of two separate Rossby waveguides (Figs. 3j).

4 Analysis of CRWP events

After having outlined the salient characteristics of the circulation patterns associated with the main modes of spectral variability, we shift our focus on CRWP events. We select events in the top and bottom 15% of each PC to study, from a composite perspective, some aspects of the origin and propagation of the associated CRWPs. The considered events have a minimum duration of five consecutive days and the minimum time separation between two consecutive events is at least of 10 days.

As a first step, we analyze the degree of zonal symmetry in the propagation of transient waves using the zonal component of the E-vector (Fig. 4). Events of particularly high PC1 and PC2 are associated with enhanced eastward propagation of transient waves, as well as with positive anomalies in RWP amplitude over a substantial portion of northern midlatitudes (Figs. 4a,c). These features, together with the peculiar projection over few, distinct (n,c_p) harmonics in the corresponding EOFs, suggest that these events correspond to CRWPs. The other sets of events do not share such characteristics: RWP amplitudes are significantly reduced over a broad portion of midlatitudes during low PC1 events (Fig. 4b), while E_x and RWP amplitude anomalies are absent or localized to smaller portions of the hemisphere for high/low PC3 or low PC2 events (Figs. 4d-f). The remaining part
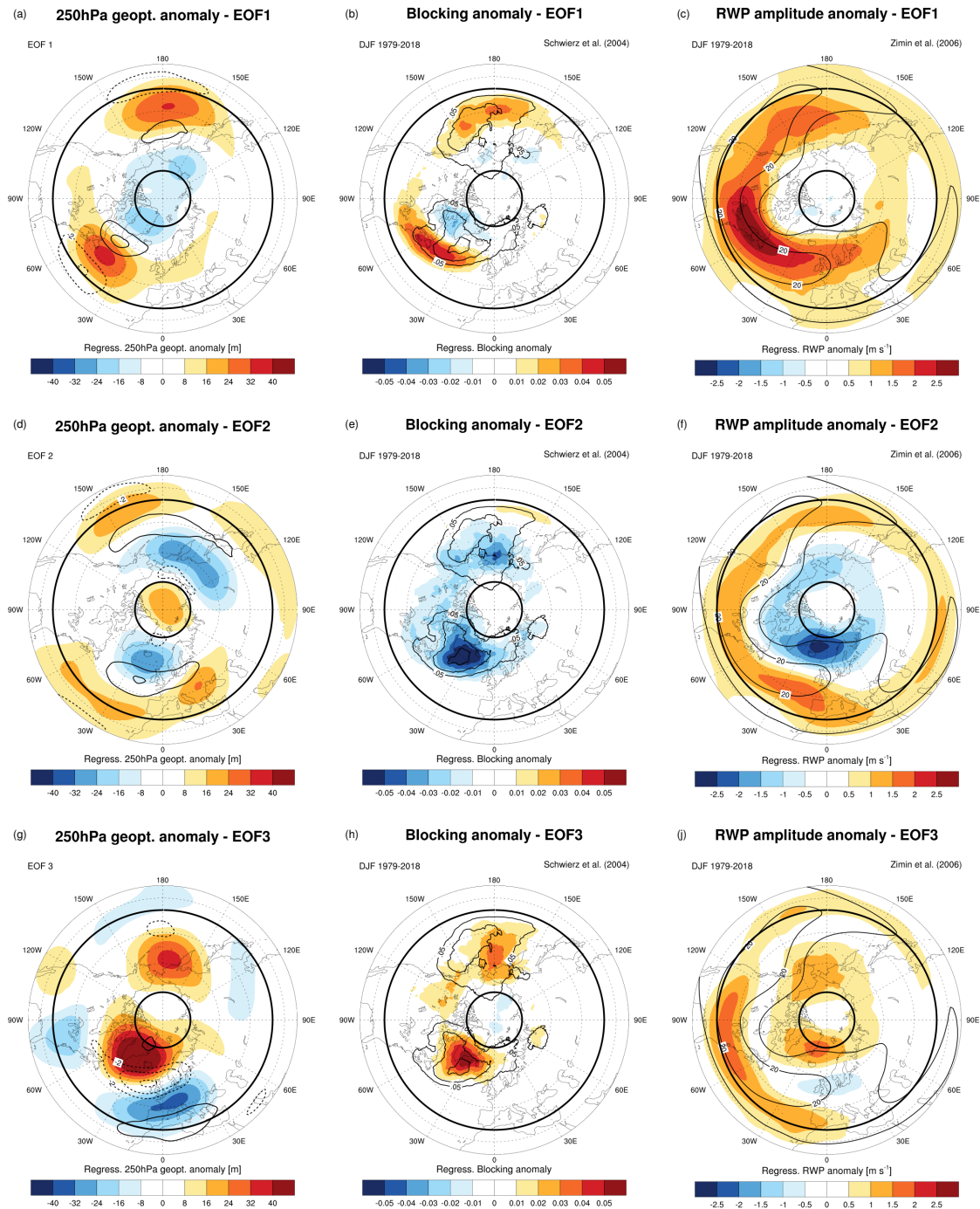
Figure 3. Linear regression of anomalies in (a,d,f) 250 hPa geopotential, (b,e,h), blocking frequency and (c,f,j) RWP amplitude with respect to the daily PC time series of (top) EOF1, (middle) EOF2, and (bottom) EOF3. The regressed 250 hPa zonal wind anomalies and the DJF climatologies of blocking and RWP amplitude are overlaid over the respective plots (black contours). Bold black latitude circles indicate 35°N and 75°N.

of the paper will then be dedicated to the analysis of the CRWPs associated with events of high PC1 and PC2, which will be

250   denoted as CRWP1 and CRWP2 (events are listed in Table S1, S2 of the Supplement).

Lagged composites of **E** and RWP amplitude anomalies are built with respect to the day of maximum PC1/PC2 in each event (t_{max}) to visualize the circumglobal character of wave propagation (Fig. 5). Their significance is assessed using a two-sided t-test with respect to the seasonal mean and variance, both extrapolated from daily data. Both CRWPs originate on the Pacific storm track as early as three days before t_{max} (Figs. 5a,e). Significant standardized anomalies of RWP and E_x

255   propagate from the Pacific to the Atlantic at time lags closer to t_{max}. Propagation occurs predominantly at high latitudes for PC1 events (Figs. 5b,c), while RWPs stay at lower latitudes during PC2 events (Figs. 5f,g) and eventually enter the subtropical jet over North Africa (Fig. 5h). It is worth of interest that both PC1 and PC2 events are associated with a stronger than usual upper-level geopotential height gradient across midlatitudes (Figs. 3a,d), a feature that can be interpreted as a proxy for the tropopause-level meridional PV gradient. This is consistent with an enhanced "waveguidability" of the large-scale flow, in the

260   sense of a configuration that favors the zonal propagation of Rossby waves (Martius et al., 2010; Wirth, 2020) and, therefore, the occurrence of CRWPs.

4.1   Origin and evolution

A first question concerns how these CRWPs are generated and in particular which processes, happening in the Tropics and/or in the extratropics, are involved.

265   **CRWP1.** The analysis of outgoing longwave radiation (OLR) during CRWP1 events highlights that tropical convection anomalies likely play a role in its initiation. Lagged composites of pentad-mean OLR indicate the presence of convective activity over the north-eastern Indian Ocean in the 10 days before t_{max} (Fig. 6a). This anomalously strong convection is the source of a negative vorticity anomaly at upper levels over the Indian subcontinent, that persists while OLR anomalies progressively decay (Fig. 6c). The same anomaly leads to an acceleration of the subtropical jet stream on its northern flank, as

270   testified by the zonal wind anomalies (Figs. 6a,c). Meanwhile, a large-scale anticyclone intensifies to the east of Japan, together with a cyclonic area in between that anticyclone and the one over the Indian subcontinent, as shown by the geopotential and vorticity anomalies (Fig. 6c). The anticyclone off the coast of Japan is the same one visible in the lagged regression analysis over the North Pacific (Fig. 3a). The arc-shape of the Rossby wave train originated from tropical convection becomes well visible more downstream, with a trough formed north of Canada and a ridge centred over Newfoundland between lags -2

275   days and +2 days (Fig. 6e). At positive lags, this Rossby wave train originating from the Tropics disappears and a more zonal propagation of wavenumbers 4 to 5 is noticeable over the midlatitudes (Figs. 6e,g).

The location of the anomalous convection and of the downstream anticyclone are reminiscent of the impact that MJO phase 3 has on the midlatitude circulation (e.g., Jeong et al., 2008; Henderson et al., 2016). To verify possible links, the median MJO amplitude in a 30-day time window centered at t_{max} is computed for CRWP1 events. Significance is assessed with

280   respect to a null distribution of 2500 randomly selected time series of median MJO amplitude, having the same length as the original one and drawn from the same number of events. The central day of each random event used to build one bootstrapped median time series is randomly selected in a 15-day time window centered on the calendar day of each t_{max} and attributed to a
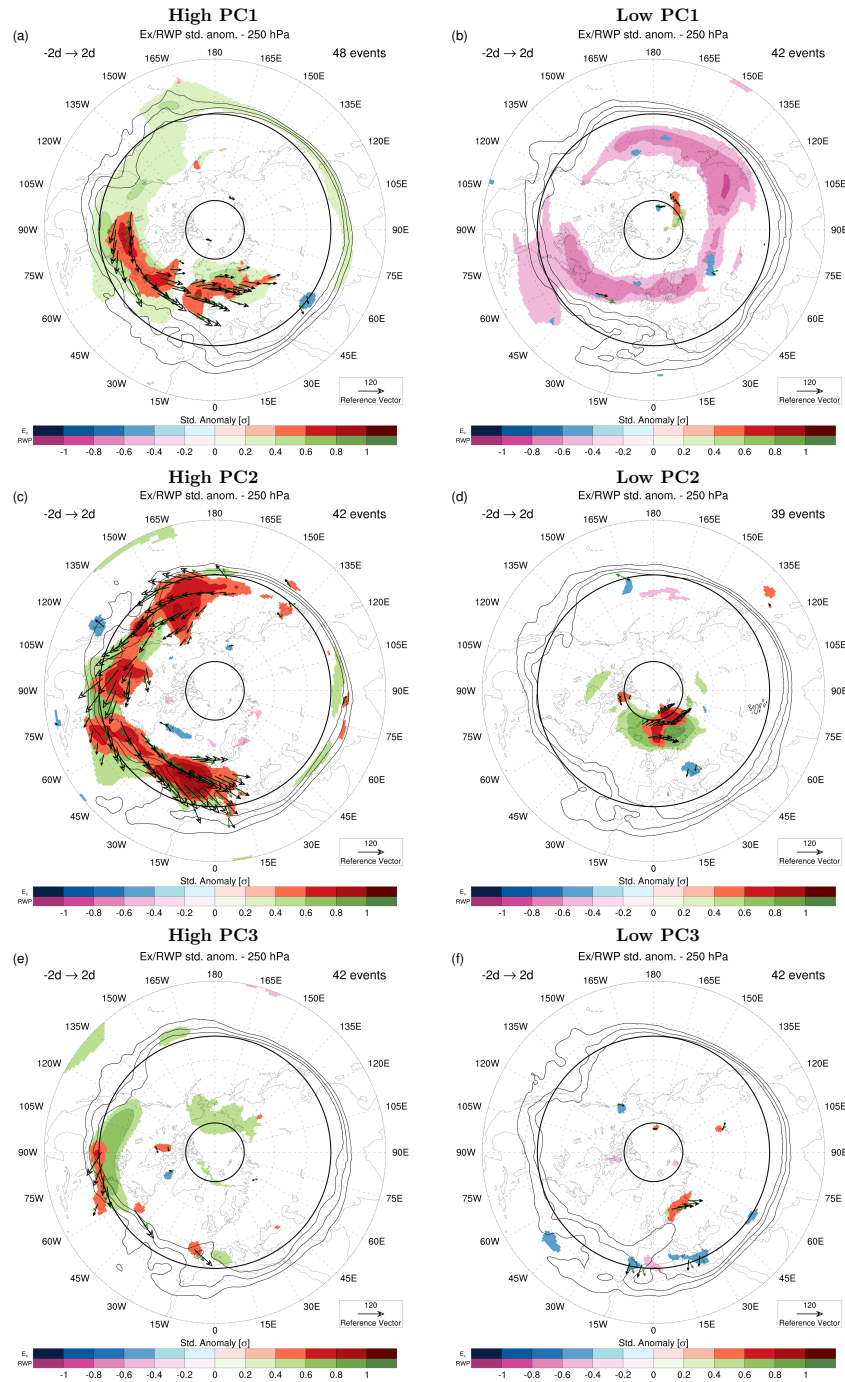
Figure 4. Composites of pentad-mean, standardized anomalies of E_x and logarithm of RWP amplitude at t_{max} of events respectively in the top and bottom 15% of (a,b) PC1 (c,d) PC2 and (e,f) PC3. Only significant standardized anomalies ($p < 0.01$) are shown, as well as composite **E** vectors (black arrows) and DJF mean **E** vectors (green arrows) emanating from areas of significant E_x anomalies. Bold black latitude circles indicate $35°$N and $75°$N.
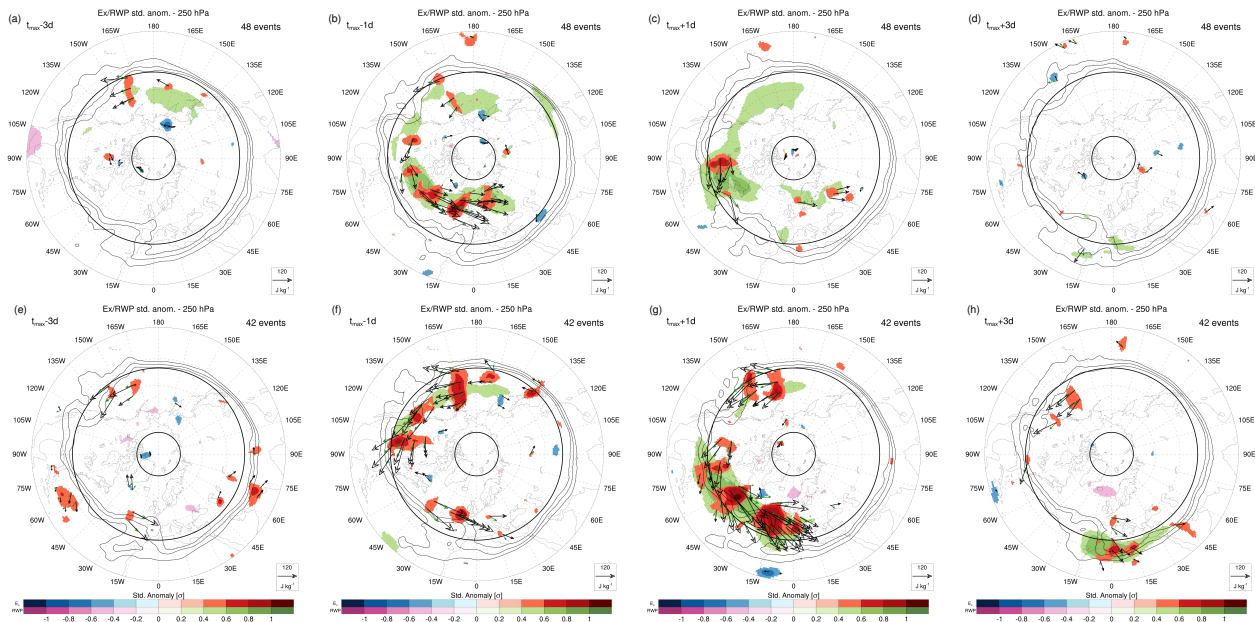
Figure 5. As in Fig. 4, but for lagged composites of daily mean, standardized anomalies of E_x and RWP amplitude, for high (top) PC1 and (bottom) PC2 events, at time lags (a,e) t_{max}-3 d (b,f) t_{max}-1 d (c,g) t_{max}+1 d and (d,h) t_{max}+3 d.

random year between 1979 and 2019 (excluding January and February 1979 and December 2019). An MJO amplitude anomaly is deemed significant if it exceeds the 90th percentile of this null distribution. A significantly amplified MJO propagating

285 between phase 3 and 4 is indeed observed 8 to 6 days before t_{max} (Figs. 7a,b). This result, though marginally significant, is consistent with the lagged composite analysis, as phase 3 corresponds to convection anomalies between India and Indonesia. The dynamical connection between an active MJO phase 3-4 and the activity of the Pacific storm track is achieved by the intensification and extension of the jet stream to the North of the diabatically influenced vorticity anomaly over the Indian subcontinent (Figs. 6a,c). This would induce quasi-geostrophic forcing for ascent and cyclogenesis at the left exit of the jet

290 and, consequently, downstream ridging related to the second anticyclone East of Japan (Jeong et al., 2008). This result is also consistent with previous work that connected phase 3 of the MJO to an enhanced activity of the North Pacific storm track (Guo et al., 2017; Zheng et al., 2018) and to a poleward displacement of the jet stream over midlatitudes, first over the Pacific and then over the Atlantic in the form of a positive phase of the North Atlantic Oscillation (NAO; e.g., Henderson et al., 2016; Lin and Brunet, 2018; Fromang and Rivière, 2020). The positive upper-level zonal wind anomalies visible over central Europe 4

295 to 8 days after t_{max} (Fig. 6j), however, are not associated with significantly positive NAO at positive lags (not shown).

CRWP2. The origin of CRWP2 does not indicate a clear influence from tropical convection: only weak OLR anomalies are observed over the Indian ocean 8 to 4 days before t_{max} (Fig. 6b), associated with a marginally significant MJO amplitude in phase 3 (Figs. 7c,d; we notice incidentally that the MJO remains active even after t_{max}). On the other hand, the Icelandic and the Aleutian low are particularly active and located more equatorward than usual in the period before t_{max} (Figs. 6d,f).
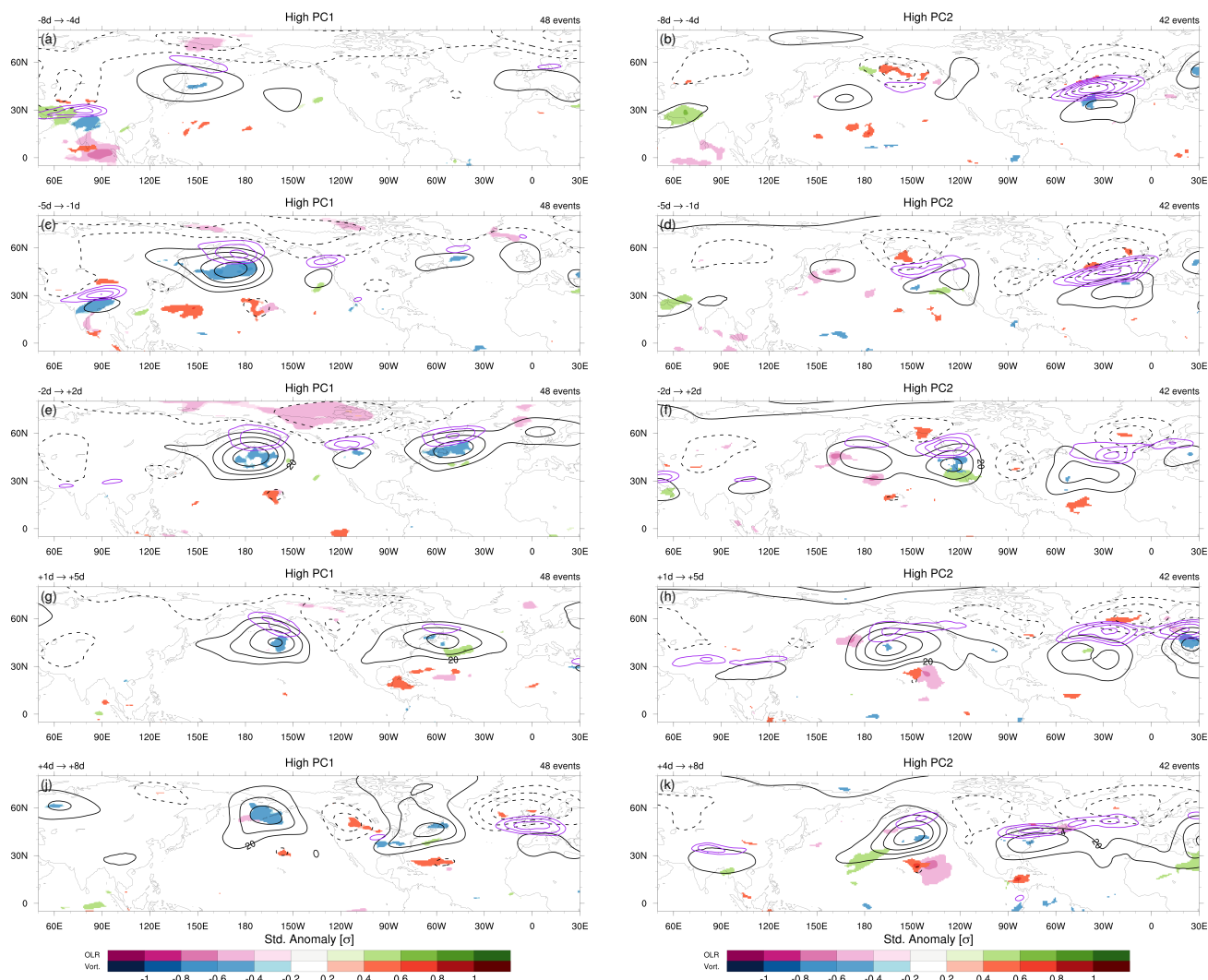
Figure 6. Lagged composites of significant ($p < 0.01$, two-sided t-test) pentad-mean standardized anomalies of OLR and 250 hPa relative vorticity (shaded) for (left) CRWP1 and (right) CRWP2 events for the pentads centered at (a,b) t_{max}-6 d (c,d) t_{max}-3 d, (e,f) t_{max}, (g,h) t_{max}+3 d and (j,k) t_{max}+6 d. Contours of pentad-mean 250 hPa geopotential height anomalies (black contours, between -80 m and +80 m every 20 m excluding zero) and positive 250 hPa zonal wind anomalies (purple contours, between 4 m s^{-1} and 7 m s^{-1} in steps of 1 m s^{-1}) are overlaid.
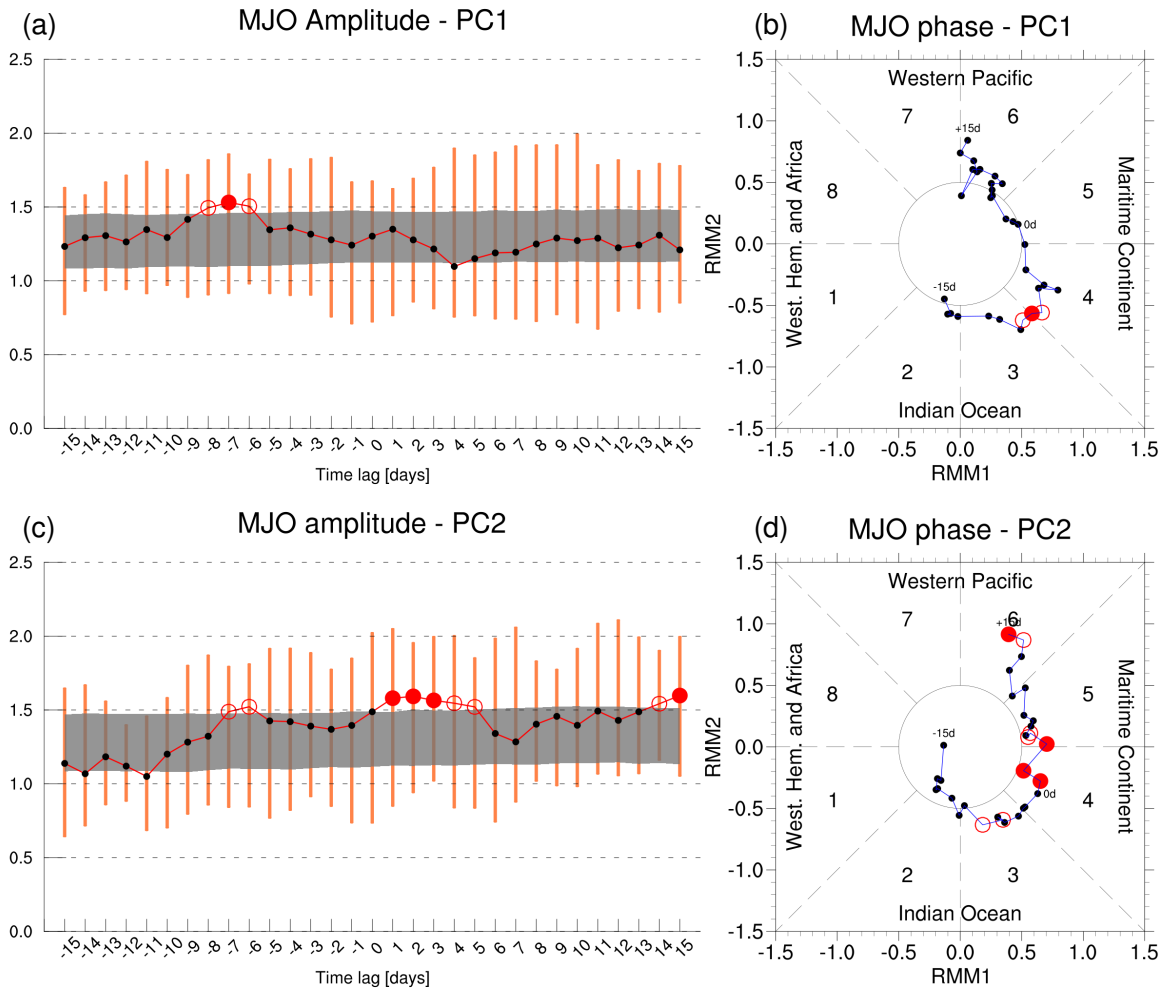
Figure 7. Time series of MJO median amplitude for the set of (a) CRWP1 and (c) CRWP2 events, evaluated between t_{max}-15 d and t_{max}+15 d (connected by red line) and of the corresponding interquartile range (orange bars). The values between the 10th and 90th percentile of the bootstrapped MJO amplitude distribution are also depicted (grey region): empty (filled) red dots indicate amplitudes exceeding the 90th (95th) percentile of the null distribution. (b, d) Median MJO components for the same set of events and period; days with significantly enhanced amplitude are highlighted as in (a,c).

300 High-latitude positive geopotential anomalies are also visible, as in the regression analysis (Fig. 3e). Although no clear trig-
gering mechanism can be pinpointed for CRWP2, we speculate that the zonal flow configuration, featuring an equatorward
displacement of both the Icelandic and Aleutian Lows and a strengthening of the upper-level geopotential gradients at their
southern side, can increase the capability of both storm tracks to zonally duct RWPs and support the occurrence of CRWPs.
The extratropical origin of CRWP2 could also be hinted by the high phase speed of the harmonics involved in it (cf. Fig. 2c),
305 while the tropical forcing leading to CRWP1 would be associated with longer time scales and, therefore, with a projection on
slower harmonics.

4.2 Effect on meridional heat flux and baroclinicity

A possible explanation about CRWP2's origin would involve a global release of accumulated baroclinicity, similar to the non-
linear oscillator mechanism described by Ambaum and Novak (2014) for the North Atlantic storm track. To test this hypothesis,
310 time series of standardized anomalies of 7-day averaged 775 hPa baroclinicity and 700 hPa transient meridional eddy heat flux
were obtained for CRWP1 and CRWP2 events. Three regions were considered for areal averaging: one corresponding to the
North Pacific storm track (130°E-180°E, 30°N-50°N), one to the North Atlantic storm track (80°W-30°W, 30°N-50°N, as
in Ambaum and Novak, 2014) and one over the 35°N-75°N latitudinal band where spectral analysis was performed (boxes
depicted in Fig. 9). As done for MJO amplitude, the median of the distributions of baroclinicity and heat flux standardized
315 anomalies were tested for significance using bootstrapping. Medians exceeding the 95th percentile of the bootstrapped distri-
bution, obtained after resampling 2500 times, were deemed significant.

CRWP1. The passage of CRWP1 is associated with significantly reduced values of baroclinicity over the two main storm
track regions: first in the North Pacific in the 8 days preceding t_{max} (Fig. 8a) and then in the North Atlantic in the eight days
after t_{max} (Fig. 8c). A significant increase in eddy meridional heat flux occurs in the same time intervals, indicating enhanced
320 poleward heat transport by baroclinic eddies. This increase is particularly strong when considering the broad 35°N-75°N
latitudinal belt, although the corresponding decrease in baroclinicity is not statistically significant (Fig. 8b). The dynamical
origin of these tendencies is explained by lagged composites of heptad-mean heat flux and baroclinicity. They illustrate how
the development of the previously discussed anticyclone over the western North Pacific coincides with significantly enhanced
meridional heat fluxes (Fig. 9a). Furthermore, the composites show that the significant reduction of baroclinicity occurs on the
325 southern side of the same anticyclone, as easterlies act to reduce the usual westerly wind shear that is present over the storm
track region. A very similar mechanism is apparent for the anticyclone subsequently developing over the North Atlantic around
t_{max}, whose development is preceded by anomalously strong meridional heat fluxes over eastern North America (Fig. 9b) and
followed by a significant reduction of baroclinicity at its southern side (Fig. 9c). The spatial pattern of meridional heat fluxes
around t_{max} resembles the one regressed onto the Northern Baroclinic Annular Mode (see Thompson and Li, 2015, their
330 Fig. 6b), sparking the hypothesis that the latter can be related to CRWP1.

CRWP2. As for CRWP1, CRWP2 events are also associated with anomalously positive peaks in meridional heat flux, first
over the North Pacific storm track (Fig. 8d) and then over the North Atlantic (Fig. 8f). These peaks are contextual to a reduction
in background baroclinicity, although no significant anomalies are detected. Lagged composites depict meridional heat flux
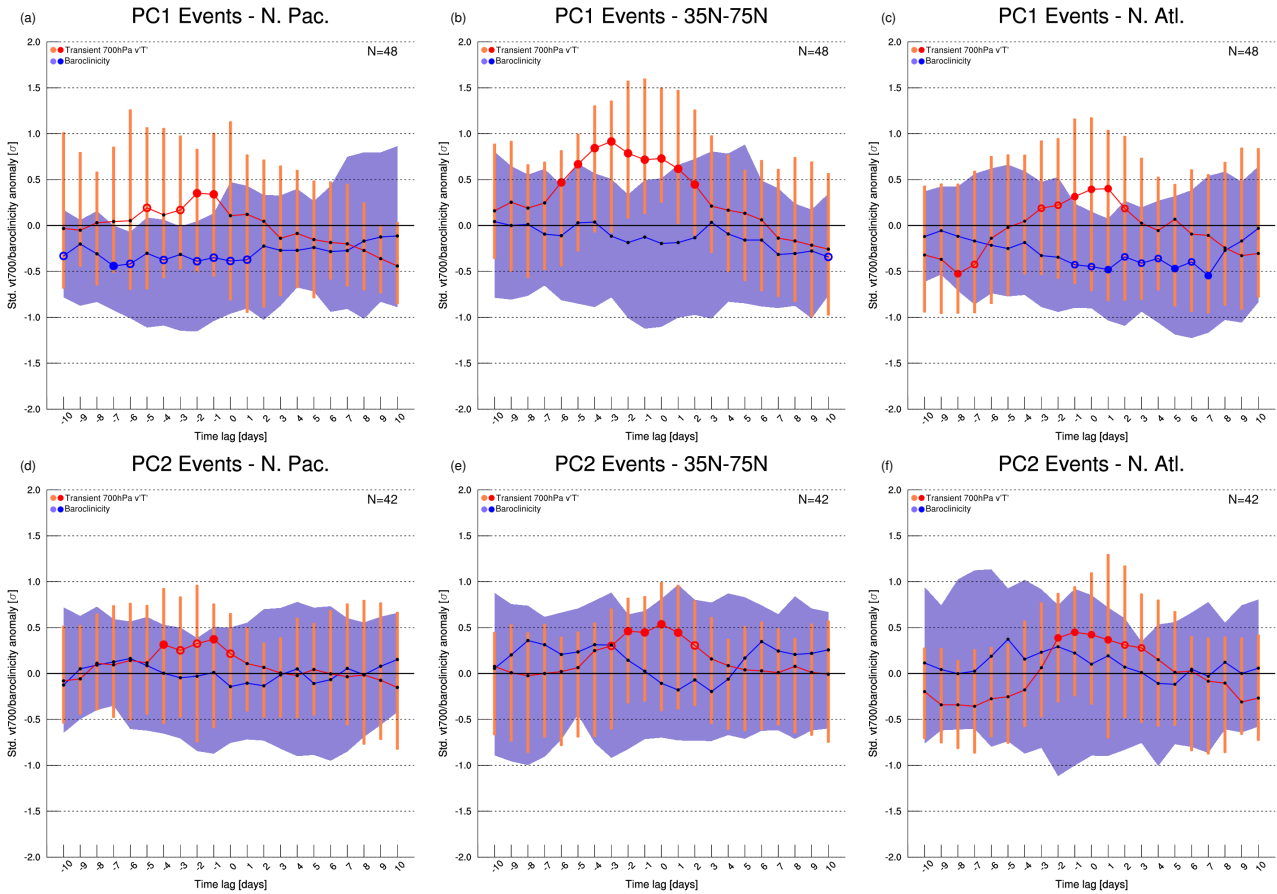
Figure 8. Medians of standardized anomalies of 7-day mean, area-averaged baroclinicity s (blue line) and meridional heat flux v^*T^* (red line) for the considered set of (top) CRWP1 and (bottom) CRWP2 events, at different lead times with respect to t_{max}, for (a,d) the North Pacific storm track (130°E-180°E, 30°N-50°N), (b,e) the whole mid-to-high latitudes (35°N-75°N) and (c,f) the North Atlantic storm track (80°W-30°W, 30°N-50°N) regions. The length of the orange bars indicates the interquartile range of the heat flux distribution, as well as the width of the blue shading for s. Empty (filled) dots indicate anomalies exceeding the 95th (99th) percentile of the respective bootstrapped distributions.

anomalies occurring first over the Pacific and then over North America, at latitudes generally lower than PC1 (Fig.,9d-e) and
335 no significant anomalies of baroclinicity in the two storm track regions.

In conclusion, results confirm the baroclinic nature of the considered CRWPs and their initiation in the North Pacific. However, the absence of a significantly positive peak in baroclinicity before t_{max} does not support the hypothesis that they are due to a hemispheric-scale discharge of previously accumulated baroclinicity.
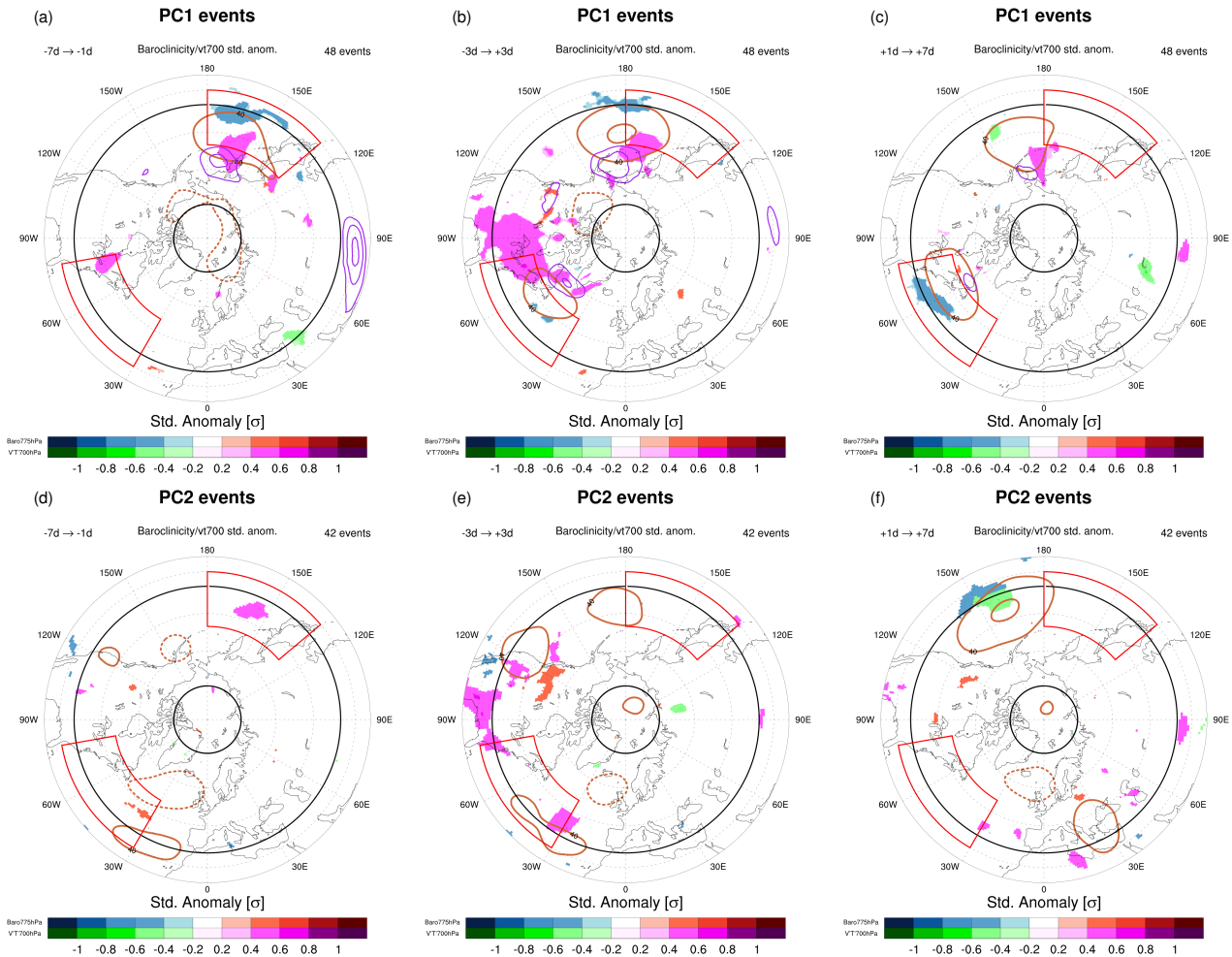
Figure 9. Lagged composites of significant ($p < 0.01$, two-sided t-test) heptad-mean standardized anomalies of 775 hPa baroclinicity and 700 hPa transient meridional heat flux (shaded), together with heptad-mean geopotential height anomalies (brown contours, only -40 m, +40 m and +80 m), for (top) CRWP1 and (bottom) CRWP2 events. The heptads centered at (a,d) t_{max}-4 d (b,e) t_{max} and (c,f) t_{max}+4 d are shown. The two storm track regions, where averaging for Fig. 8 was performed, are indicated in red. Bold black latitude circles indicate 35°N and 75°N.

4.3 Propagation to the subtropical jet

340 Lagged composites highlight that enhanced RWP amplitudes persist over North Africa and the middle East at positive lags, while their amplitude keeps decreasing elsewhere (Figs. 5d,h). This would suggest a propagation of RWPs from the midlatitude jet over the Atlantic to the subtropical jet over North Africa. To verify this hypothesis, composites of **E** vector, RWP amplitude and PV are computed for the considered set of events in the days following t_{max}.

The propagation of CRWP2 and, although to a minor extent, of CRWP1 is associated with significant negative anomalies
345 of the meridional component of **E**, indicating positive momentum fluxes and enhanced anticyclonic orientation of transient eddies at the entrance of the subtropical jet over the Iberian Peninsula and western North Africa (Fig. 10). Following the close link between the group velocity direction relative to the mean flow and the E-vector (Hoskins et al., 1983), the significant anomalies of E_y logically co-occur with the equatorward propagation of significant RWP amplitude anomalies from the North Atlantic to North Africa as seen in the lagged composites of E_y between t_{max}+1d and t_{max}+3d (Figs. 10a-f). The transfer
350 of RWPs from the North Atlantic to the subtropical jet bears some resemblance with one of the case studies discussed by Ahmadi-Givi et al. (2014) and confirms the role played by anticyclonic wave breaking to "close the circle" and connect the Atlantic with the Pacific storm track via the subtropical jet. This result is in agreement with Branstator (2002), who identified a circumglobal teleconnection from a PC analysis over a low-latitude region occupied by the subtropical jet (0-45°N,0-120°E), apparently unrelated to the main storm tracks. Similarly, Davies (2015) was able to close their "weather chain" by tracking
355 wind anomalies at low latitudes along the subtropical jet back to the Pacific storm track, imposing to their pattern a periodicity of around 10 days.

5 Conclusions and outlook

Wavenumber/phase speed spectral analysis can provide a compact characterization of the Rossby waves propagating above Northern Hemispheric midlatitudes in a given time interval. It allows to assess which harmonics contribute the most to the
360 evolution of the hemispheric flow pattern, evaluating its shape and zonal propagation at the same time. This approach provides a favorable framework to study CRWPs, as the Rossby wave trains constituting them project clearly on distinct harmonics in the spectral domain. We compiled a climatology of the spectral signatures of midlatitude Rossby waves and let CRWPs emerge from it as variability patterns with a prominent, well-defined signal in the spectral domain. The first two spectral variability patterns identified with this approach are indeed related to the zonal propagation of significantly amplified, transient
365 Rossby waves over a significant portion of the hemisphere. Such CRWPs are embedded in a hemisperic-scale circulation pattern characterized by enhanced upper-tropospheric, meridional gradients of geopotential height. We reiterate that these CRWPs emerge from the analysis of spectral properties of midlatitude Rossby waves, without imposing any explicit constraint about the waveguidability of the hemispheric flow configuration. This fact assures that CRWPs are a natural circumglobal teleconnection occurring during boreal winter over northern midlatitudes and not a methodological artifact.
370 The first mode of spectral variability during boreal winter corresponds to an eastward-traveling CRWP stretching from the Pacific to the Atlantic storm track and that involves exclusively zonal wavenumbers between $n = 4$ and $n = 6$. The second
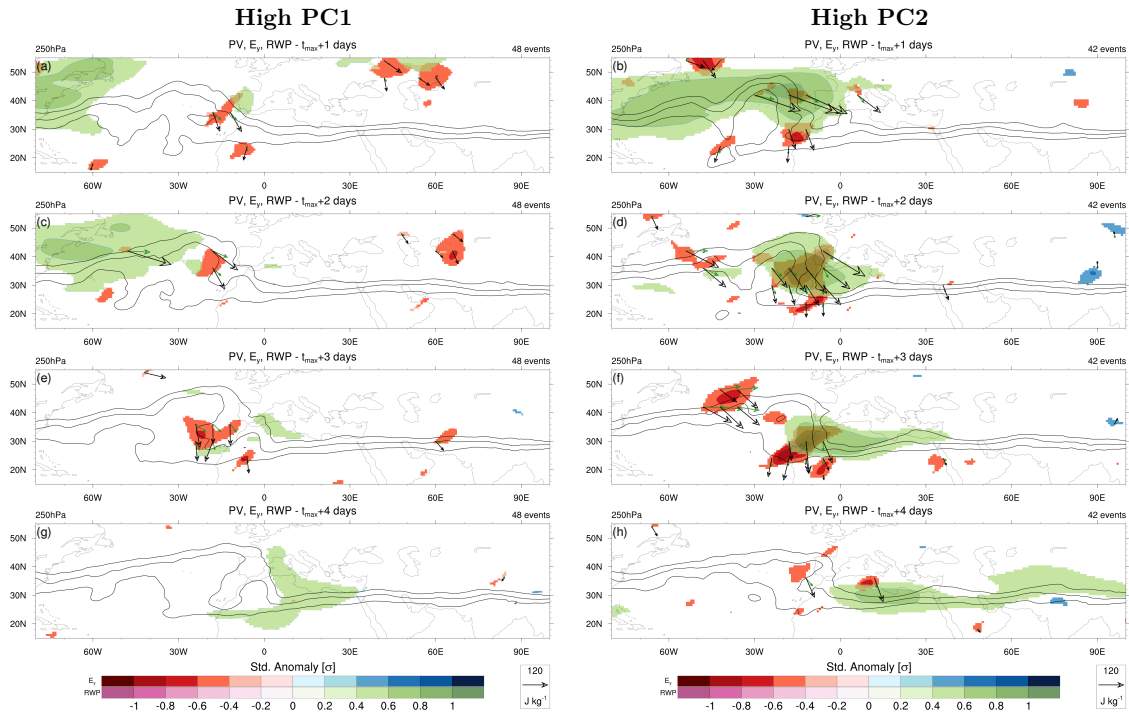
Figure 10. Lagged composites of significant ($p < 0.01$) 250 hPa standardized anomalies in E_y (red for anticyclonic tilt, blue for cyclonic tilt of transient eddies) and logarithm of RWP amplitude (green for positive, magenta for negative values) for (left) CRWP1 and (right) CRWP2 events, at (a,b) +1 days, (c,d) +2 days, (e,f) +3 days, (g,h) +4 days with respect to t_{max}. The composite of PV at 250 hPa is overlaid (black contours, only 1 PVU, 1.5 PVU and 2 PVU), as well as the composite **E** vectors (black arrows) and DJF mean **E** vectors (green arrows) emanating from areas of significant E_y anomalies.

mode of spectral variability features a selective enhancement of wavenumbers larger or equal than $n = 6$ concomitant to a suppression of slow harmonics with lower wavenumbers, and it corresponds to the rapid eastward propagation of a CRWP over lower midlatitudes. The CRWPs related to these two modes are identified respectively as CRWP1 and CRWP2.

375   The analyzed CRWPs share some common features and bear some differences. Both originate first in the North Pacific storm track and then propagate to the North Atlantic one. Their propagation is associated with positive anomaly of low-level meridional heat flux over the same regions, which is indicative of the baroclinic activity associated with the traveling Rossby wave packets. Both CRWPs, but in particular CRWP2, propagate from the North Atlantic to the subtropical jet via anticyclonic wave breaking over North Africa, suggesting a potential role of the subtropical jet as a "connector" between the Atlantic and

380   the Pacific storm tracks. Speaking of differences between the two patterns, CRWP2 propagates at overall lower latitudes and its propagation is more rapid than for CRWP1. The main difference, however, lies in their origin: tropical convection in the Indian Ocean likely plays an important role in the initiation of CRWP1, as testified by the significant OLR anomalies registered in the region before CRWP1 events and by the similarity of the circulation pattern to the one following strong MJO events in phase 3. The origin of CRWP2 is less clear, although CRWP2 events occur together with a concomitant equatorward displacement of

385 the jet stream over the two storm track regions. We speculate that this configuration might promote the occurrence of CRWPs; this hypothesis can be investigated in future work assessing which properties of the large-scale flow can promote circumglobal wave propagation.

A similar analysis to the one performed in this piece of work can be proposed for boreal summer to study warm-season CRWPs: however, the applicability of spectral analysis might be hindered by the weaker storm track activity with respect to

390 winter (Hoskins and Hodges, 2019a, b). Overall, this study is a first effort to systematically connect midlatitude circulation variability at the hemispheric scale with its spectral signature. This fingerprint of the large-scale circulation can be employed to characterize the shape and propagation of Rossby waves in a global fashion, without the need of filtering, and pave the way to new quantitative tools (as the global phase speed metric developed by Riboldi et al., 2020). Being applied on gridded output of standard meteorological quantities, the method can be easily implemented in climate models to highlight potential biases in

395 the representation of CRWPs or other circulation features, like atmospheric blocking, and assess their potential modifications under different global warming scenarios.

Author contributions. JR developed the concept of the project, executed the analysis and wrote the manuscript. All the authors followed the project and supported its technical implementation and the interpretation of the results.

Competing interests. The authors declare no competing interests.

400 *Acknowledgements.* The atmospheric blocking data set has been kindly provided by the Institute of Atmospheric and Climate Science of ETH Zurich. The authors would also like to thank Dim Coumou and Gabriele Messori for the feedback on previous version of this work. This work was supported by funding from the JPI-Climate/Belmont Forum project GOTHAM (ANR-15-JCLI-0004-01 and 01LP1611A).

References

Ahmadi-Givi, F., Nasr-Esfahany, M., and Mohebalhojeh, A. R.: Interaction of North Atlantic baroclinic wave packets and the Mediterranean storm track, Quart. J. Roy. Meteor. Soc., 140, 754–765, https://doi.org/https://doi.org/10.1002/qj.2171, 2014.

Altenhoff, A. M., Martius, O., Croci-Maspoli, M., Schwierz, C., and Davies, H. C.: Linkage of atmospheric blocks and synoptic-scale Rossby waves: a climatological analysis, Tellus A, 60, 1053–1063, https://doi.org/10.1111/j.1600-0870.2008.00354.x, 2008.

Ambaum, M. H. P. and Novak, L.: A nonlinear oscillator describing storm track variability, Quart. J. Roy. Meteor. Soc., 140, 2680–2684, https://doi.org/https://doi.org/10.1002/qj.2352, 2014.

Branstator, G.: Circumglobal teleconnections, the jet stream Waveguide, and the North Atlantic Oscillation, J. Climate, 15, 1893–1910, https://doi.org/10.1175/1520-0442(2002)015<1893:CTTJSW>2.0.CO;2, 2002.

Cassou, C.: Intraseasonal interaction between the Madden—Julian Oscillation and the North Atlantic Oscillation, Nature, pp. 523–527, https://doi.org/10.1038/nature07286, 2008.

Chang, E. K. M., Lee, S., and Swanson, K. L.: Storm Track Dynamics, J. Climate, 15, 2163–2183, https://doi.org/10.1175/1520-0442(2002)015<02163:STD>2.0.CO;2, 2002.

Cooley, J. W. and Tukey, J. W.: An algorithm for the machine calculation of complex Fourier series, Math. Comp., 19, 297–301, https://doi.org/doi.org/10.1090/S0025-5718-1965-0178586-1, 1965.

Coumou, D., Petoukhov, V., Rahmstorf, S., Petri, S., and Schellnhuber, H. J.: Quasi-resonant circulation regimes and hemispheric synchronization of extreme weather in boreal summer, Proc. Nat. Academy Sci., 111, 12 331–12 336, https://doi.org/10.1073/pnas.1412797111, 2014.

Davies, H.: Weather chains during the 2013/2014 winter and their significance for seasonal prediction, Nature Geosci., 8, 833–837, https://doi.org/10.1038/ngeo2561, 2015.

Davini, P., Cagnazzo, C., Gualdi, S., and Navarra, A.: Bidimensional diagnostics, variability, and trends of Northern Hemisphere blocking, J. Climate, 25, 6496–6509, https://doi.org/10.1175/JCLI-D-12-00032.1, 2012.

Dee, D. P., Uppala, S. M., Simmons, A. J., Berrisford, P., Poli, P., Kobayashi, S., Andrae, U., Balmaseda, M. A., Balsamo, G., Bauer, P., Bechtold, P., Beljaars, A. C. M., van de Berg, L., Bidlot, J., Bormann, N., Delsol, C., Dragani, R., Fuentes, M., Geer, A. J., Haimberger, L., Healy, S. B., Hersbach, H., Holm, E. V., Isaksen, L., Kallberg, P., Köhler, M., Matricardi, M., McNally, A. P., Monge-Sanz, B. M., Morcette, J.-J., Park, B.-K., Peubey, C., de Rosnay, P., Tavolato, C., Thepaut, J.-N., and Vitart, F.: The ERA-Interim reanalysis: Configuration and performance of the data assimilation system, Quart. J. Roy. Meteor. Soc., 137, 553–597, https://doi.org/DOI:10.1002/qj.828, 2011.

Dell'Aquila, A., Lucarini, V., Ruti, P., and Calmanti, S.: Hayashi spectra of the Northern Hemisphere mid-latitude atmospheric variability in the NCEP-NCAR and ECMWF reanalyses, Clim. Dyn., 25, 639–652, https://doi.org/10.1007/s00382-005-0048-x, 2005.

Ferranti, L., Magnusson, L., Vitart, F., and Richardson, D. S.: How far in advance can we predict changes in large-scale flow leading to severe cold conditions over Europe?, Quart. J. Roy. Meteor. Soc., 144, 1788–1802, https://doi.org/https://doi.org/10.1002/qj.3341, 2018.

Franzke, C., Fraedrich, K., and Lunkeit, F.: Low-frequency variability in a simplified atmospheric global circulation model: Storm-track induced 'spatial resonance', Quart. J. Roy. Meteor. Soc., 126, 2691–2708, https://doi.org/10.1002/qj.49712656905, 2006.

Fromang, S. and Rivière, G.: The effect of the Madden–Julian Oscillation on the North Atlantic Oscillation using idealized numerical experiments, J. Atmos. Sci., 77, 1613–1635, https://doi.org/10.1175/JAS-D-19-0178.1, 2020.

Gollan, G., Bastin, S., and Greatbatch, R. J.: Tropical precipitation influencing boreal winter midlatitude blocking, Atmos. Sci. Lett., 20,
440   e900, https://doi.org/https://doi.org/10.1002/asl.900, 2019.

Grise, K. M., Son, S.-W., and Gyakum, J. R.: Intraseasonal and interannual variability in North American storm tracks and its relationship to
        equatorial Pacific variability, Mon. Wea. Rev., 141, 3610–3625, https://doi.org/10.1175/MWR-D-12-00322.1, 2013.

Guo, Y., Shinoda, T., Lin, J., and Chang, E. K. M.: Variations of Northern Hemisphere storm track and extratropical cyclone activity associ-
        ated with the Madden–Julian Oscillation, J. Climate, 30, 4799–4818, https://doi.org/10.1175/JCLI-D-16-0513.1, 2017.

445 Hakim, G. J.: Developing wave packets in the North Pacific storm track, Mon. Wea. Rev., 131, 2824–2837, https://doi.org/10.1175/1520-
        0493(2003)131<2824:DWPITN>2.0.CO;2, 2003.

Hartmann, D. L.: Pacific sea surface temperature and the winter of 2014, Geophys. Res. Lett., 42, 1894–1902,
        https://doi.org/10.1002/2015GL063083, 2015.

Henderson, S. A., Maloney, E. D., and Barnes, E. A.: The influence of the Madden–Julian Oscillation on Northern Hemisphere winter
450   blocking, J. Climate, 29, 4597–4616, https://doi.org/10.1175/JCLI-D-15-0502.1, 2016.

Hoskins, B. J. and Ambrizzi, T.: Rossby Wave Propagation on a Realistic Longitudinally Varying Flow, J. Atmos. Sci., 50, 1661–1671,
        https://doi.org/10.1175/1520-0469(1993)0502.0.CO;2, 1993.

Hoskins, B. J. and Hodges, K. I.: The annual cycle of Northern Hemisphere storm tracks. Part I: Seasons, J. Climate, 32, 1743–1760,
        https://doi.org/10.1175/JCLI-D-17-0870.1, 2019a.

455 Hoskins, B. J. and Hodges, K. I.: The annual cycle of Northern Hemisphere storm tracks. Part II: Regional Detail, J. Climate, 32, 1761–1775,
        https://doi.org/10.1175/JCLI-D-17-0871.1, 2019b.

Hoskins, B. J. and Karoly, D. J.: The steady linear response of a spherical atmosphere to thermal and orographic Forcing, J. Atmos. Sci., 38,
        1179–1196, https://doi.org/10.1175/1520-0469(1981)038<1179:TSLROA>2.0.CO;2, 1981.

Hoskins, B. J. and Valdes, P. J.: On the existence of Storm-Tracks, J. Atmos. Sci., 47, 1854–1864, https://doi.org/10.1175/1520-
460   0469(1990)047<1854:OTEOST>2.0.CO;2, 1990.

Hoskins, B. J., James, I. N., and White, G. H.: The shape, propagation and mean-flow interaction of large-scale weather systems, J. Atmos.
        Sci., 40, 1595–1612, https://doi.org/10.1175/1520-0469(1983)040<1595:TSPAMF>2.0.CO;2, 1983.

Jeong, J.-H., Kim, B.-M., Ho, C.-H., and Noh, Y.-H.: Systematic Variation in Wintertime Precipitation in East Asia by MJO-Induced Extrat-
        ropical Vertical Motion, J.Climate, 21, 788–801, https://doi.org/10.1175/2007JCLI1801.1, 2008.

465 Jolly, E., D'Andrea, F., Rivière, G., and Fromang, S.: Linking Warm Arctic Winters, Rossby Waves, and Cold Spells: An Idealized Numerical
        Study, J. Atmos. Sci., 78, 2783–2799, https://doi.org/10.1175/JAS-D-20-0088.1, 2021.

Kornhuber, K., Petoukhov, V., Petri, S., Rahmstorf, S., and Coumou, D.: Evidence for wave resonance as a key mechanism for generating
        high–amplitude quasi–stationary waves in boreal summer, Clim. Dyn., 49, 1961–1979, https://doi.org/10.1007/s00382-016-3399-6, 2017.

Kornhuber, K., Osprey, S., Coumou, D., Petri, S., Petoukhov, V., Rahmstorf, S., and Gray, L.: Extreme weather events in early summer 2018
470   connected by a recurrent hemispheric wave-7 pattern, Environ. Res. Lett., 14, 054 002, https://doi.org/10.1088/1748-9326/ab13bf, 2019.

Lee, S. and Held, I. M.: Baroclinic wave packets in models and observations, J. Atmos. Sci., 50, 1413–1428, https://doi.org/10.1175/1520-
        0469(1993)0502.0.CO;2, 1993.

Lin, H. and Brunet, G.: Extratropical response to the MJO: Nonlinearity and sensitivity to the initial State, J. Atmos. Sci., 75, 219–234,
        https://doi.org/10.1175/JAS-D-17-0189.1, 2018.

475 Lott, F., Kuttippurath, J., and Vial, F.: A Climatology of the gravest waves in the equatorial lower and middle stratosphere: Method and
        results for the ERA-40 Re-Analysis and the LMDz GCM, J. Atmos. Sci., 66, 1327–1346, https://doi.org/10.1175/2008JAS2880.1, 2009.

Mann, M. E., Rahmstorf, S., Kornhuber, K., Steinman, B. A., Miller, S. K., Petri, S., and Coumou, D.: Projected changes in persistent extreme summer weather events: The role of quasi-resonant amplification, Science Advances, 4, https://doi.org/10.1126/sciadv.aat3272, 2018.

Martineau, P., Chen, G., and Burrows, D. A.: Wave Events: Climatology, Trends, and Relationship to Northern Hemisphere Winter Blocking and Weather Extremes, J. Climate, 30, 5675–5697, https://doi.org/10.1175/JCLI-D-16-0692.1, 2017.

Martius, O., Schwierz, C., and Davies, H. C.: Tropopause-Level Waveguides, J. Atmos. Sci., 67, 866–879, https://doi.org/10.1175/2009JAS2995.1, 2010.

Pelly, J. L. and Hoskins, B. J.: A new perspective on blocking, J. Atmos. Sci., 60, 743–755, https://doi.org/10.1175/1520-0469(2003)060<0743:ANPOB>2.0.CO;2, 2003.

Petoukhov, V., Rahmstorf, S., Petri, S., and Schellnhuber, H. J.: Quasiresonant amplification of planetary waves and recent Northern Hemisphere weather extremes, Proc. Nat. Acad. Sci., 110, 5336–5341, https://doi.org/10.1073/pnas.1222000110, 2013.

Randel, W. J. and Held, I. M.: Phase speed spectra of transient eddy fluxes and critical layer absorption, J. Atmos. Sci., 48, 688–697, https://doi.org/10.1175/1520-0469(1991)048<0688:PSSOTE>2.0.CO;2, 1991.

Riboldi, J., Grams, C. M., Riemer, M., and Archambault, H. M.: A phase locking perspective on Rossby wave amplification and atmospheric blocking downstream of eecurving western North Pacific tropical cyclones, Mon. Wea. Rev., 147, 567–589, https://doi.org/10.1175/MWR-D-18-0271.1, 2019.

Riboldi, J., Lott, F., D'Andrea, F., and Rivière, G.: On the linkage between Rossby wave phase speed, atmospheric blocking and Arctic Amplification, in review at Geophys. Res. Lett., 2020.

Rivière, G. and Drouard, M.: Dynamics of the Northern Annular Mode at Weekly Time Scales, J. Atmos. Sci., 72, 4569–4590, https://doi.org/10.1175/JAS-D-15-0069.1, 2015.

Rossby, C.-G.: Planetary flow patterns in the atmosphere, Quart. J. Roy. Meteor. Soc., 66, 68–87, 1940.

Schemm, S. and Schneider, T.: Eddy lifetime, number, and diffusivity and the suppression of eddy kinetic energy in midwinter, J. Climate, 31, 5649–5665, https://doi.org/10.1175/JCLI-D-17-0644.1, 2018.

Schemm, S., Rivière, G., Ciasto, L. M., and Li, C.: Extratropical cyclogenesis changes in connection with tropospheric ENSO teleconnections to the North Atlantic: Role of stationary and transient Waves, J. Atmos. Sci., 75, 3943–3964, https://doi.org/10.1175/JAS-D-17-0340.1, 2018.

Schemm, S., Wernli, H., and Binder, H.: The storm-track suppression over the western North Pacific from a cyclone life-cycle perspective, Weather Clim. Dynam., 2, 55–69, https://doi.org/10.5194/wcd-2-55-2021, 2021.

Schwierz, C., Croci-Maspoli, M., and Davies, H. C.: Perspicacious indicators of atmospheric blocking, Geophys. Res. Lett., 31, https://doi.org/10.1029/2003GL019341, l06125, 2004.

Shutts, G. J.: The propagation of eddies in diffluent jetstreams: Eddy vorticity forcing of 'blocking' flow fields, Quart. J. Roy. Meteor. Soc., 109, 737–761, https://doi.org/10.1002/qj.49710946204, 1983.

Sussman, H., Raghavendra, A., Roundy, P., and Dai, A.: Trends in northern midlatitude atmospheric wave power from 1950 to 2099, Clim. Dyn., 54, 2903–2918, https://doi.org/10.1007/s00382-020-05143-3, 2020.

Teng, H. and Branstator, G.: Amplification of Waveguide Teleconnections in the Boreal Summer, Curr. Clim. Change Rep., 5, 421–432, https://doi.org/doi.org/10.1007/s40641-019-00150-x, 2019.

Thompson, D. W. J. and Li, Y.: Baroclinic and Barotropic Annular Variability in the Northern Hemisphere, J. Atmos. Sci., 72, 1117–1136, https://doi.org/10.1175/JAS-D-14-0104.1, 2015.

Tibaldi, S. and Molteni, F.: On the operational predictability of blocking, Tellus A, 42, 343–365,
515   https://doi.org/https://doi.org/10.1034/j.1600-0870.1990.t01-2-00003.x, 1990.

Trenberth, K. E.: An assessment of the impact of transient eddies on the zonal flow during a blocking episode using localized Eliassen–Palm
    flux diagnostics, J. Atmos. Sci., 43, 2070–2087, https://doi.org/10.1175/1520-0469(1986)043<2070:AAOTIO>2.0.CO;2, 1986.

Wang, S.-Y., Hipps, L., Gillies, R. R., and Yoon, J.-H.: Probable causes of the abnormal ridge accompanying the 2013-
    –2014 California drought: ENSO precursor and anthropogenic warming footprint, Geophys. Res. Lett., 41, 3220–3226,
520   https://doi.org/10.1002/2014GL059748, 2014.

Wheeler, M. and Kiladis, G. N.: Convectively coupled equatorial waves: Analysis of clouds and temperature in the wavenumber–frequency
    Domain, J. Atmos. Sci., 56, 374–399, https://doi.org/10.1175/1520-0469(1999)056<0374:CCEWAO>2.0.CO;2, 1999.

Wirth, V.: Waveguidability of idealized midlatitude jets and the limitations of ray tracing theory, Weather Clim. Dynam., 1, 111–125,
    https://doi.org/10.5194/wcd-1-111-2020, 2020.

525   Wirth, V. and Polster, C.: The problem of diagnosing jet waveguidability in the presence of large-amplitude eddies, J. Atmos. Sci.",
    https://doi.org/10.1175/JAS-D-20-0292.1, 2021.

Wirth, V., Riemer, M., Chang, E. K. M., and Martius, O.: Rossby wave packets on the midlatitude waveguide – A review, Mon. Wea. Rev.,
    146, 1965–2001, https://doi.org/10.1175/MWR-D-16-0483.1, 2018.

Woollings, T. and Hoskins, B.: Simultaneous Atlantic—Pacific blocking and the Northern Annular Mode, Quart. J. Roy. Meteor. Soc., 134,
530   1635–1646, https://doi.org/10.1002/qj.310, 2008.

Xu, P., Wang, L., Vallis, G. K., Geen, R., Screen, J. A., Wu, P., Ding, S., Huang, P., and Chen, W.: Amplified Waveguide Teleconnections
    Along the Polar Front Jet Favor Summer Temperature Extremes Over Northern Eurasia, Geophys. Res. Lett., 48, e2021GL093 735, 2021.

Yang, S., Reinhold, B., and Källén, E.: Multiple Weather Regimes and Baroclinically Forced Spherical Resonance, J. Atmos. Sci., 54,
    1397–1409, https://doi.org/10.1175/1520-0469(1997)054<1397:MWRABF>2.0.CO;2, 1997.

535   Zheng, C., Kar-Man Chang, E., Kim, H.-M., Zhang, M., and Wang, W.: Impacts of the Madden–Julian Oscillation on storm-track Activity,
    surface air temperature, and precipitation over North America, J. Climate, 31, 6113–6134, https://doi.org/10.1175/JCLI-D-17-0534.1,
    2018.

Zimin, A. V., Szunyogh, I., Hunt, B. R., and Ott, E.: Extracting envelopes of nonzonally propagating Rossby wave packets, Mon. Wea. Rev.,
    134, 1329–1333, https://doi.org/10.1175/MWR3122.1, 2006.